STRAIN AND TEMPERATURE ENGINEERING OF ENERGY STORAGE PERFORMANCE IN FERROELECTRIC/PARAELECTRIC SUPERLATTICES

Ha Thi Dang[1,2], Dang Thi Hong Hue[3], Ba-Hieu Vu[3], Trong-Giang Nguyen[3], Van-Hai Dinh[3], Le Van Lich[3]*

[1]*Vietnam National University of Forestry, Hanoi, Vietnam*
[2]*PhD student in Materials Engineering, Hanoi University of Science and Technology, Hanoi, Vietnam*
[3]*Hanoi University of Science and Technology, Hanoi, Vietnam*

*Corresponding author: lich.levan@hust.edu.vn

(Received: May 03, 2025; Revised: June 18, 2025; Accepted: June 19, 2025)

DOI: 10.31130/ud-jst.2025.23(9B).516E

Abstract - This study investigates the effects of biaxial strain and temperature on polarization domains and energy storage properties of lead titanate/strontium titanate superlattices through phase-field simulations. The superlattice exhibits periodic polarization vortices with alternating symmetries, whose distribution is strain-dependent: compressive strain enlarges vortex regions, while tensile strain suppresses them, favoring uniform alignment. These domain reconfigurations govern hysteresis, with compressive strain yielding single-loop and tensile strain producing double-loop polarization–electric field responses. Energy storage performance exhibits strong strain dependence, under tensile strain achieving optimal discharge energy density of 74.03 J/cm³ and efficiency of 99.74%, a 25% enhancement over compressive conditions. Thermal analysis confirms stable energy storage up to 500°C, highlighting operational robustness. By correlating mechanical-thermal stimuli with domain evolution, this work establishes strain engineering as an effective strategy for designing ferroelectric superlattices with on-demand energy storage capabilities, advancing the development of adaptive dielectric capacitors.

Key words – Energy storage; Ferroelectric/paraelectric nanocomposite; Domain structure; Phase field model.

1. Introduction

Dielectric capacitors are essential components in electrical and electronic systems due to their ability to rapidly charge and discharge, enabling ultrahigh power density, durability, and high operational voltage [1]-[3]. These devices store energy electrostatically through polarization, where an applied electric field displaces dipoles in the material. Optimal energy storage performance-characterized by high energy density, efficiency, and low loss-requires materials with a significant maximum polarization (P_m) and minimal remanent polarization (P_r) after field removal. Thin-film capacitors have gained prominence for their superior breakdown strength and suitability for compact, miniaturized systems [4], [5]. In ferroelectric (FE) materials, domain structure critically influences P_m and P_r. By introducing compositional complexity, long-range ferroelectric domains can be fragmented into polar nanoregions, which exhibit dynamic switching under electric fields with reduced energy dissipation [6]-[9]. This approach has enabled energy-storage densities exceeding 50 J/cm^3 and efficiencies of 60–80% [10]-[12].

Advances in nanofabrication have facilitated the development of artificial superlattices, which combine alternating ferroelectric and dielectric layers with thicknesses less than 10 nm to engineer novel properties. Such heterostructures, including $BaTiO_3/SrTiO_3$, $BiFeO_3/SrTiO_3$, and $PbTiO_3/SrTiO_3$ (PTO/STO) systems, exhibit enhanced responses to external stimuli like electric fields and strain, often leading to emergent phenomena such as polar vortices, skyrmions, and flux-closure domains [13]-[20]. For instance, PTO/STO superlattices have demonstrated unique polarization behaviors, including improper ferroelectricity and smoothly evolving nanostructures, depending on layer periodicity and strain conditions [15]-[19]. However, research on how strain and temperature influence domain configurations and energy storage performance in these systems remains limited.

This study employs phase-field simulations to investigate domain structure formation in PTO/STO superlattices, focusing on strain and temperature effects. By analyzing polarization-electric field (P-E) hysteresis loops, the work quantifies energy storage metrics such as discharge energy density and charge-discharge efficiency, providing insights into how tailored domain engineering can optimize energy storage performance. The simulations reveal the evolution of domain patterns under varying conditions, bridging gaps in understanding the interplay between external parameters and functional properties in superlattice-based capacitors.

2. Methodology

2.1. Free energy of $PbTiO_3/SrTiO_3$ superlattice

This study employs a phase-field modeling approach to analyze domain configurations and energy storage potential in ferroelectric/paraelectric PTO/STO superlattices. The framework utilizes the polarization vector $P(p_1, p_2, p_3)$ to describe domain patterns and their dynamic response to applied fields. The system's total energy (H) is determined through the integration of energy density (h) across the material volume (V):

$$H = \int h dV = \int [(1-f)h^{PTO} + f h^{STO}] dV \quad (1)$$

where the phase parameter f distinguishes between composite constituents: $f = 0$ represents pure PTO, while $f = 1$ corresponds to pure STO. Here, h^{PTO} and h^{STO} denote the energy densities of PTO and STO, respectively. The PTO energy density incorporates contributions from Landau free energy, elastic interactions, gradient energy, and electrostatic effects.

$$h^{BTO} = \alpha_i^{PTO} p_i^2 + \alpha_{ij}^{PTO} p_i^2 p_j^2 + \alpha_{ijk}^{PTO} p_i^2 p_j^2 p_k^2 + \frac{1}{2} c_{ijkl}^{PTO} [\varepsilon_{ij} - \varepsilon_{ij}^0][\varepsilon_{kl} - \varepsilon_{kl}^0] + G_{ijkl}^{PTO} p_{i,j} p_{k,l} - \frac{1}{2} k_c^{PTO} E_i^2 - E_i p_i \quad (2)$$

where $\varepsilon_{ij}^0 = Q_{ijkl} p_k p_l$ refers to the spontaneous strain induced by polarization, with Q_{ijkl} denoting electrostrictive coefficients. Similarly, the total energy density of STO comprises Landau, elastic, gradient energy, and electric densities, which can be expressed as

$$h^{STO} = \alpha_i^{STO} p_i^2 + \alpha_{ij}^{STO} p_i^2 p_j^2 + \alpha_{ijk}^{STO} p_i^2 p_j^2 p_k^2 + \frac{1}{2} c_{ijkl}^{STO} [\varepsilon_{ij} - \varepsilon_{ij}^0][\varepsilon_{kl} - \varepsilon_{kl}^0] + G_{ijkl}^{STO} p_{i,j} p_{k,l} - \frac{1}{2} k_c^{STO} E_i^2 - E_i p_i \quad (3)$$

In Eqs. (2) and (3), α_i, α_{ij}, and α_{ijk} represent thermodynamic (or Landau) coefficients; c_{ijkl} are elastic coefficients, G_{ijkl} are gradient coefficients; and k_c is the dielectric parameter. In addition, the energy term ($G_{ijkl} p_{i,j} p_{k,l}$) describes polarization gradient energy density, which is induced by spatial polarization variation, such as domain walls.

2.2. The equilibrium and governing equations

Mechanical equilibrium is governed by the stress balance equation:

$$\nabla \cdot \sigma = \frac{\partial}{\partial x_j} \left(\frac{\partial h}{\partial \varepsilon_{ij}} \right) = 0 \quad (4)$$

where σ represents the stress tensor. Electrical equilibrium satisfies the relation:

$$\epsilon_0 \epsilon_{ij}^b \nabla_i \nabla_j \phi = p_{i,i}, \quad (5)$$

Here, ϕ denotes the electrostatic potential, ϵ_0 is the vacuum permittivity, and ϵ_{ij}^b corresponds to the relative background permittivity. Polarization dynamics over time are modeled via the time-dependent Ginzburg-Landau equation:

$$\frac{\partial p_i(x_j,t)}{\partial t} = -M \frac{\delta H}{\delta p_i(x_j,t)} \quad (6)$$

where M is the mobility coefficient and t represents the evolution time.

2.3. Simulation models and procedures

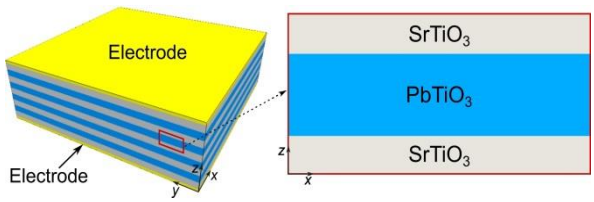

Figure 1. *Schematic illustrations of $PbTiO_3/SrTiO_3$ multilayer*

This work examines a ferroelectric/dielectric PTO/STO superlattice system. The structure comprises alternating PTO and STO nanolayers of equal thickness of 8 nm, as illustrated in Figure 1, with both materials occupying 50% of the total volume. The computational model spans 16 nm × 16 nm × 16 nm. Prior experimental works [15]-[19] have demonstrated the feasibility of fabricating such superlattices with precise layer control. This study concentrates on the effects of biaxial strain within the *xy*-plane (varied from -1% to 1%) and temperature (ranging from 0°C to 500°C) on domain structures and energy storage performance.

A uniform grid ($\Delta x = \Delta y = \Delta z = 0.4$ nm) is used to discretize the simulation model. The *x*-, *y*-, and *z*-axes align with the [100], [010], and [001] crystallographic directions, respectively. Periodic boundary conditions are applied along all three axes. Material parameters for PTO and STO are adapted from previous studies [21]-[25]. To isolate strain effects, simulations fix temperature at 25°C; conversely, temperature-dependent analyses maintain zero applied strain.

Equilibrium domain configurations are determined by numerically solving the time-dependent Ginzburg-Landau equation. Starting from an initial polarization state with minor random perturbations, iterations proceed until the system's free energy stabilizes. The semi-implicit Fourier spectral technique [26], [27] facilitates temporal integration. Following equilibrium attainment, a quasi-static electric field is applied along the *z*-axis to probe polarization response and switching dynamics.

3. Results and discussion

3.1. Polarization domain structures

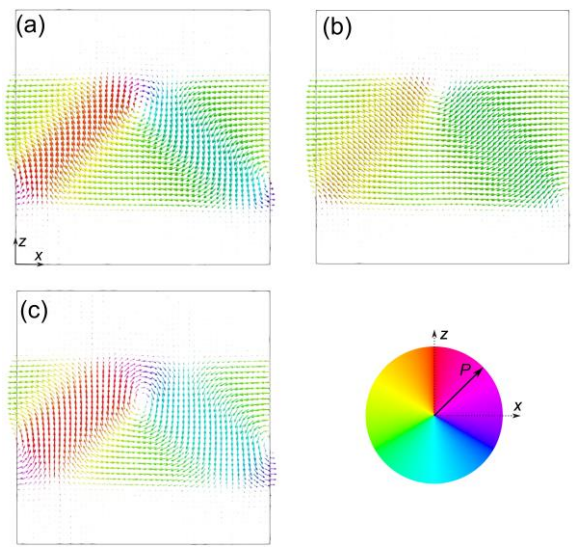

Figure 2. *Domain structures of $PbTiO_3/SrTiO_3$ superlattice under different biaxial strains: (a) ε = 0 %, (b) ε = 1 %, and (c) ε = -1 %*

Figure 2 illustrates the strain-dependent polarization patterns in a cross-sectional view of the PTO/STO superlattice. At zero applied strain (ε = 0%), the system stabilizes into a periodic vortex array at room temperature, with vortex cores localized near the PTO/STO interfacial regions (Figure 2a). These observations align with prior experimental and computational findings [15]-[19], confirming strain-free vortex self-organization in such superlattices.

Applying tensile strain (ε = 1%) reduces vortex dimensions, relocating cores closer to the PTO/STO interfaces (Figure 2b). Conversely, compressive strain (ε = −1%) enlarges the vortex diameter, displacing core positions toward the central regions of the PTO layers (Figure 2c). This strain-mediated core displacement arises

from competing polarization-strain coupling effects, where tensile strain promotes in-plane polarization alignment (enhancing *xy*-plane dipole ordering), while compressive strain favors out-of-plane orientation, amplifying vertical polarization gradients and expanding vortex geometries. These results demonstrate that biaxial strain exerts substantial control over domain structures in ferroelectric superlattices.

3.2. Polarization switching and energy-storage performance of strained PTO/STO superlattice

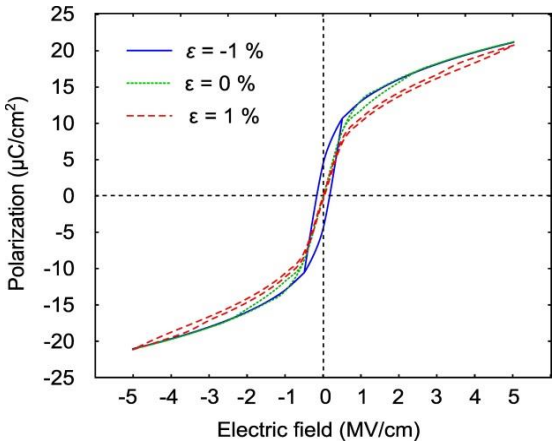

Figure 3. *Polarization-electric field behaviors of $PbTiO_3/SrTiO_3$ superlattice under an applied electric field of 5 MV/cm at different strains*

Figure 3 compares the strain-dependent polarization-electric field (P_3-E_3) hysteresis responses of the PTO/STO superlattice. Under -1% compressive strain, the system displays a wide hysteresis loop, characteristic of robust ferroelectricity with high remanent polarization. This indicates that the compressive strain stabilizes a strong ferroelectric phase within the superlattice, aligning the polarization along the out-of-plane direction. At zero strain, however, the loop adopts a double hysteresis shape, signaling antiferroelectric-like ordering - a notable feature given the non-antiferroelectric nature of the constituent materials. This suggests that at zero strain, the system enters a more complex polarization state, involving alternating vortices with opposite polarization directions or the formation of nanoscale domains that effectively cancel each other out at a macroscopic level. This dual-loop behavior is also observed in the superlattice subjected to the tensile strain of 1 %, albeit with potentially different switching fields and saturation polarization values compared to the zero-strain case. The emergence of this antiferroelectric-like behavior under tensile strain suggests that the strain induces a structural change within the superlattice, leading to the formation of an antipolar phase. This could be due to the tensile strain encouraging a different stacking arrangement of the PTO and STO layers that influence the polarization behavior. Further analysis, such as examining the atomic displacements and local polarization profiles, would be necessary to fully elucidate the microscopic mechanisms driving these strain-dependent polarization transitions.

The energy storage performance of the PTO/STO superlattice is considered. Theoretically, the energy storage performance can be evaluated by

$$U_c = \int_0^{p_m} Edp \tag{7}$$

$$U_d = \int_{p_r}^{p_m} Edp \tag{8}$$

$$\eta = \frac{U_d}{U_c} \times 100\% \tag{9}$$

Here, U_c, U_d, and η correspond to the total stored energy, retrievable energy, and charge-discharge efficiency, respectively. Ferroelectric systems with large hysteresis loops exhibit significant energy dissipation ($U_{loss} = U_c - U_d$), making η a critical metric for evaluating practical energy utilization. The energy density is governed by both polarization magnitude and hysteresis loop, with narrower loops favoring higher efficiency.

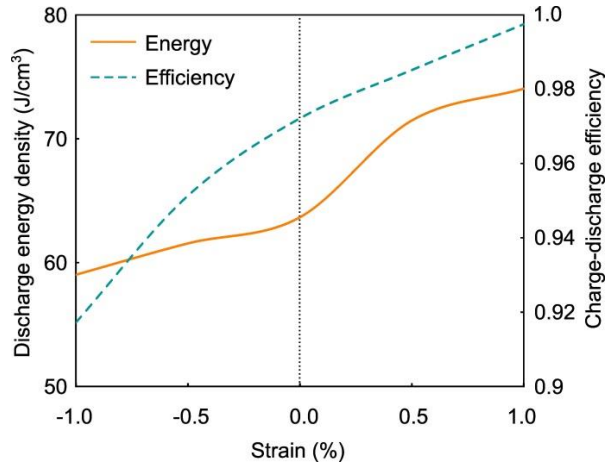

Figure 4. *Discharge energy density and charge–discharge efficiency of $PbTiO_3/SrTiO_3$ superlattice at various biaxial strains*

Figure 4 analyzes the strain-dependent trends in discharge energy density for the PTO/STO superlattice during electric-field-driven recovery (5 MV/cm). Both discharge energy density (U_d) and energy efficiency (η) exhibit a monotonic relationship with applied strain as they rise with increasing tensile strain but decline under compressive conditions. Notably, the system reaches a U_d of 74.03 J/cm^3 (η = 99.74%) at 1% tensile strain, demonstrating near-ideal energy recovery. Conversely, at -1% compression, U_d drops to 59.02 J/cm^3 (η = 91.72%), reflecting heightened hysteresis losses. Between these extremes, the strain-free configuration achieves U_d=63.64 J/cm^3 (η = 97.21%). The superlattice exhibits a 25% enhancement in U_d observed across the −1% to +1% strain range. This improvement under tension stems from suppressed hysteresis (reduced polarization remanent), which minimizes energy dissipation during charge-discharge cycles.

3.3. Effect of temperature on polarization switching and energy-storage performance of PTO/STO superlattice

Figure 5 displays the temperature-dependent polarization-electric field hysteresis loops (P_3-E_3) for the PTO/STO superlattice, with biaxial strain effects excluded from the analysis to isolate the impact of temperature alone. The characteristic double hysteresis loop emerges at 0°C, indicating the presence of an antiferroelectric-like phase due to the formation of an

alternative vortex array at low temperatures. This double loop progressively narrows with rising temperatures, suggesting a weakening of the antiferroelectric-like order as thermal energy increases. The complete disappearance of the double hysteresis loop above 350°C signifies a transition to a paraelectric phase, where the material loses its long-range polar order. At elevated temperatures (>350°C), the P_3-E_3 curves transition to nonlinear behavior without observable hysteresis, consistent with a paraelectric state where the polarization response is primarily electronic and easily reversible. Notably, the maximum polarization under a 5 MV/cm applied field shows a systematic reduction with increasing thermal energy. This is attributed to the increased randomization of dipoles at higher temperatures, making it more difficult for the electric field to align them effectively. The reduction in maximum polarization further supports the transition from an ordered (antiferroelectric-like or ferroelectric) state to a disordered paraelectric state. These results demonstrate significant temperature sensitivity in both the hysteretic characteristics and polarization magnitude of the superlattice system, highlighting the potential for temperature-controlled switching and tuning of its dielectric properties. The observed temperature dependence could be related to changes in the lattice parameters, thermal expansion differences between PTO and STO, or thermally activated defect migration, each of which could influence the polarization behavior.

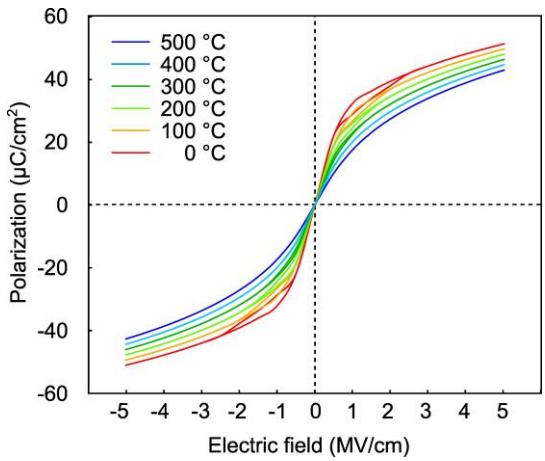

Figure 5. *Polarization-electric field behaviors of $PbTiO_3$/$SrTiO_3$ superlattice under an applied electric field of 5 MV/cm at different temperatures*

Figure 6 demonstrates the temperature-dependent evolution of discharge energy density and charge-discharge energy efficiency in the PTO/STO superlattice during electric-field-driven recovery (5 MV/cm) from poled states. The discharge energy density shows systematic enhancement with thermal activation, increasing from 63.0 J/cm^3 at 0°C to 73.68 J/cm^3 at 500°C, which is a 17% relative improvement across this operational range. Simultaneously, energy efficiency exhibits progressive thermal optimization, achieving complete energy recovery (100%) at 400°C and maintaining this ideal performance up to 500°C. This coupled temperature response reveals coordinated thermal activation mechanisms governing both energy storage capacity and conversion effectiveness in the superlattice system.

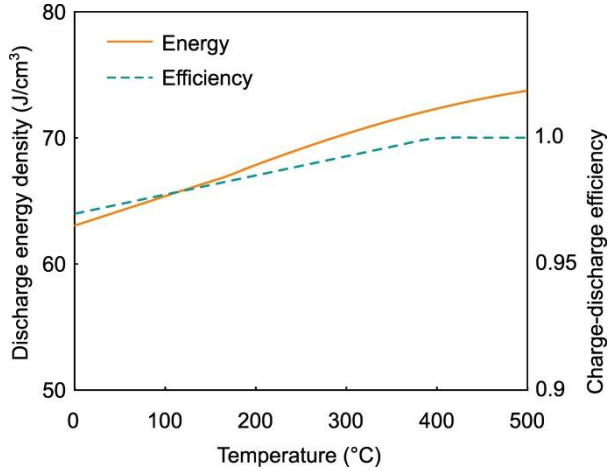

Figure 6. *Discharge energy density and charge–discharge efficiency of $PbTiO_3$/$SrTiO_3$ superlattice at various temperatures*

4. Conclusion

This investigation establishes biaxial strain and thermal modulation as critical determinants of domain structures and energy storage capabilities in PTO/STO superlattices through phase-field modeling. The system hosts an ordered polarization vortex lattice with alternating chirality, demonstrating strain-mediated structural control, where vortex domains expand under compressive strain while contracting under tensile loading. These reconfigurations directly govern hysteretic responses, manifesting as single-loop ferroelectric switching under compression versus double-loop characteristics in tensile regimes. Energy storage performance reveals asymmetric strain dependence, with significant enhancement under tensile strain versus marked degradation under compression. Thermal analysis demonstrates retained functional stability up to 500°C with near-ideal efficiency. These findings establish precise strain engineering coupled with thermal management as a dual-parameter optimization strategy for tailoring vortex-mediated energy storage in artificial superlattices.

Acknowledgments: This research is funded by Vietnam National Foundation for Science and Technology Development (NAFOSTED) under Grant Number 103.02–2021.79.

REFERENCES

[1] H. Palneedi, M. Peddigari, G. T. Hwang, D. Y. Jeong, and J. Ryu, "High-performance dielectric ceramic films for energy storage capacitors: progress and outlook", *Advanced Functional Materials*, vol. 28, no. 42, pp. 1803665, 2018. https://doi.org/10.1002/adfm.201803665

[2] L. Yang *et al.*, "Perovskite lead-free dielectrics for energy storage applications", *Progress in Materials Science*, vol. 102, pp. 72-108, 2019. https://doi.org/10.1016/j.pmatsci.2018.12.005

[3] G. Wang *et al.*, "Electroceramics for high-energy density capacitors: current status and future perspectives", *Chemical Reviews*, vol. 121, no. 10, pp. 6124-6172, 2021.

https://doi.org/10.1021/acs.chemrev.0c01264

[4] H. Pan *et al.*, "Ultrahigh–energy density lead-free dielectric films via polymorphic nanodomain design", *Science*, vol. 365, no. 6453, pp. 578-582, 2019. DOI: 10.1126/science.aaw8109

[5] J. Kim, *et al.*, "Ultrahigh capacitive energy density in ion-bombarded relaxor ferroelectric films", *Science*, vol. 369, no. 6499, pp. 81-84, 2020. DOI: 10.1126/science.abb0631

[6] L.E. Cross, "Relaxor ferroelectrics", *Ferroelectrics*, vol. 76, no. 1, pp. 241-267, 1987. https://doi.org/10.1080/00150198708016945

[7] A. Bokov and Z.-G. Ye, "Recent progress in relaxor ferroelectrics with perovskite structure", *Journal of materials science*, vol. 41, no. 1, pp. 31-52, 2006. https://doi.org/10.1007/s10853-005-5915-7

[8] F. Li *et al.*, "Ultrahigh piezoelectricity in ferroelectric ceramics by design", *Nature materials*, vol. 17, no. 4, pp. 349-354, 2018. https://doi.org/10.1038/s41563-018-0034-4

[9] F. Li *et al.*, "The origin of ultrahigh piezoelectricity in relaxor-ferroelectric solid solution crystals", *Nature communications*, vol. 7, no. 1, pp. 13807, 2016. https://doi.org/10.1038/ncomms13807

[10] H. Pan *et al.*, "$BiFeO_3$–$SrTiO_3$ thin film as a new lead-free relaxor-ferroelectric capacitor with ultrahigh energy storage performance", *Journal of Materials Chemistry A*, vol. 5, no. 12, pp. 5920-5926, 2017. https://doi.org/10.1039/C7TA00665A

[11] K. Wang *et al.*, "Superparaelectric $(Ba_{0.95}, Sr_{0.05})(Zr_{0.2},Ti_{0.8})O_3$ ultracapacitors", *Advanced Energy Materials*, vol. 10, no. 37, pp. 2001778, 2020. https://doi.org/10.1002/aenm.202001778

[12] H. Pan *et al.*, "Giant energy density and high efficiency achieved in bismuth ferrite-based film capacitors via domain engineering", *Nature communications*, vol. 9, no. 1, pp. 1813, 2018. https://doi.org/10.1038/s41467-018-04189-6

[13] Y. Tang *et al.*, "Observation of a periodic array of flux-closure quadrants in strained ferroelectric $PbTiO_3$ films", *Science*, vol. 348, no. 6234, pp. 547-551, 2015. DOI: 10.1126/science.1259869

[14] Z. Hong *et al.*, "Stability of polar vortex lattice in ferroelectric superlattices", *Nano letters*, vol. 17, no. 4, pp. 2246-2252, 2017. https://doi.org/10.1021/acs.nanolett.6b04875

[15] A. Yadav *et al.*, "Observation of polar vortices in oxide superlattices", *Nature*, vol. 530, no. 7589, pp. 198-201, 2016. https://doi.org/10.1038/nature16463

[16] S.L. Hsu *et al.*, "Emergence of the vortex state in confined ferroelectric heterostructures", *Advanced materials*, vol. 31, no. 36, pp. 1901014, 2019. https://doi.org/10.1002/adma.201901014

[17] A.Y. Abid *et al.*, "Creating polar antivortex in $PbTiO_3$/$SrTiO_3$ superlattice", *Nature Communications*, vol. 12, no. 1, pp. 2054, 2021. https://doi.org/10.1038/s41467-021-22356-0

[18] S. Das *et al.*, "Observation of room-temperature polar skyrmions", *Nature*, vol. 568, no. 7752, pp. 368-372, 2019. https://doi.org/10.1038/s41586-019-1092-8

[19] F.-H. Gong *et al.*, "Atomic mapping of periodic dipole waves in ferroelectric oxide", *Science Advances*, vol. 7, no. 28, pp. eabg5503, 2021. DOI: 10.1126/sciadv.abg5503

[20] Y. Wang *et al.*, "Polar meron lattice in strained oxide ferroelectrics", *Nature Materials*, vol. 19, no. 8, pp. 881-886, 2020. https://doi.org/10.1038/s41563-020-0694-8

[21] L.V. Lich *et al.*, "Anomalous toughening in nanoscale ferroelectrics with polarization vortices", *Acta materialia*, vol. 88, pp. 147-155, 2015. https://doi.org/10.1016/j.actamat.2014.12.056

[22] L.V. Lich *et al.*, "Continuum thermodynamics of unusual domain evolution-induced toughening effect in nanocracked strontium titanate", *Engineering Fracture Mechanics*, vol. 190, pp. 232-244, 2018. https://doi.org/10.1016/j.engfracmech.2017.12.030

[23] N. Pertsev, A. Tagantsev, and N. Setter, "Phase transitions and strain-induced ferroelectricity in $SrTiO_3$ epitaxial thin films", *Physical review B*, vol. 61, no. 2, pp. R825, 2000. https://doi.org/10.1103/PhysRevB.61.R825

[24] H. Uwe and T. Sakudo, "Stress-induced ferroelectricity and soft phonon modes in $SrTiO_3$", *Physical Review B*, vol. 13, no. 1, pp. 271, 1976. https://doi.org/10.1103/PhysRevB.13.271

[25] A.K. Tagantsev, E. Courtens, and L. Arzel, "Prediction of a low-temperature ferroelectric instability in antiphase domain boundaries of strontium titanate", *Physical Review B*, vol. 64, no. 22, pp. 224107, 2001. https://doi.org/10.1103/PhysRevB.64.224107

[26] Y.H. Huang *et al.*, "Thermodynamic and phase-field studies of phase transitions, domain structures, and switching for $Ba(Zr_xTi_{1-x})O_3$ solid solutions", *Acta Mater*, vol. 186, pp. 609-615, 2020. https://doi.org/10.1016/j.actamat.2020.01.019

[27] L.V. Lich *et al.*, "Low-field energy storage enhancement in ferroelectric/paraelectric $PbTiO_3$/$SrTiO_3$ nanocomposites near antiferroelectric–ferroelectric transition region", *Journal of Science: Advanced Materials Devices*, vol. 9, no. 2, pp. 100687, 2024. https://doi.org/10.1016/j.jsamd.2024.100687